



**HAL**  
open science

## In Situ Observation of Solar-flare-induced Proton Cyclotron Waves Upstream from Mars

Haibo Lin, Jianpeng Guo, Kei Masunaga, Kanako Seki, Christian Mazelle,  
Dan Zhao, Hui Huang, Juan Zhao, Yong Wei, Libo Liu

► **To cite this version:**

Haibo Lin, Jianpeng Guo, Kei Masunaga, Kanako Seki, Christian Mazelle, et al.. In Situ Observation of Solar-flare-induced Proton Cyclotron Waves Upstream from Mars. *The Astrophysical Journal*, 2022, 934, 10.3847/1538-4357/ac7d4f. insu-03867478

**HAL Id: insu-03867478**

**<https://insu.hal.science/insu-03867478>**

Submitted on 23 Nov 2022

**HAL** is a multi-disciplinary open access archive for the deposit and dissemination of scientific research documents, whether they are published or not. The documents may come from teaching and research institutions in France or abroad, or from public or private research centers.

L'archive ouverte pluridisciplinaire **HAL**, est destinée au dépôt et à la diffusion de documents scientifiques de niveau recherche, publiés ou non, émanant des établissements d'enseignement et de recherche français ou étrangers, des laboratoires publics ou privés.



Distributed under a Creative Commons Attribution 4.0 International License



# In Situ Observation of Solar-flare-induced Proton Cyclotron Waves Upstream from Mars

Haibo Lin<sup>1</sup>, Jianpeng Guo<sup>1</sup>, Kei Masunaga<sup>2</sup>, Kanako Seki<sup>3</sup>, Christian Mazelle<sup>4</sup>, Dan Zhao<sup>1</sup>, Hui Huang<sup>1</sup>,  
Juan Zhao<sup>1</sup>, Yong Wei<sup>5</sup>, and Libo Liu<sup>5,6,7</sup>

<sup>1</sup> Planetary and Space Physics Group, Department of Astronomy, Beijing Normal University, Beijing 100875, People's Republic of China; [jpguo@bnu.edu.cn](mailto:jpguo@bnu.edu.cn)

<sup>2</sup> Institute of Space and Astronautical Science, Japan Aerospace Exploration Agency, Kanagawa 252-5210, Japan

<sup>3</sup> Department of Earth and Planetary Science, Graduate School of Science, University of Tokyo, Tokyo 113-0033, Japan

<sup>4</sup> IRAP CNRS-University of Toulouse-UPS-CNES, PEPS, Toulouse, France

<sup>5</sup> Key Laboratory of Earth and Planetary Physics, Institute of Geology and Geophysics, Chinese Academy of Sciences, Beijing 100029, People's Republic of China

<sup>6</sup> Heilongjiang Mohe Observatory of Geophysics, Institute of Geology and Geophysics, Chinese Academy of Sciences, Beijing 100029, People's Republic of China

<sup>7</sup> College of Earth and Planetary Sciences, University of Chinese Academy of Sciences, Beijing 100049, People's Republic of China

Received 2022 April 28; revised 2022 June 26; accepted 2022 June 28; published 2022 August 5

## Abstract

Proton cyclotron waves (PCWs) upstream from Mars are usually interpreted as waves generated by ion/ion instabilities due to the interaction between the solar wind plasma and the pickup protons, originating from the extended hydrogen (H) exosphere of Mars. Their generation mainly depends on the solar wind properties and the relative density of the newborn protons with respect to the background solar wind. Under stable solar wind conditions, a higher solar irradiance leads to both increased exospheric H density and ionization rate of H atoms, and therefore a higher relative density, which tends to increase the linear wave growth rate. Here we show that the solar irradiance is likely to contribute significantly to PCW generation. Specifically, we present observations from the Mars Atmosphere and Volatile Evolution (MAVEN) spacecraft indicating that, around the peak of the X8.2 flare on 2017 September 10, the increased solar irradiance gave rise to higher pickup H<sup>+</sup> fluxes, which in turn excited PCWs. This result has implications for inferring the loss of hydrogen to space in early Martian history with more intense and frequent X-class flares as well as their contributions to the total loss.

*Unified Astronomy Thesaurus concepts:* [Solar wind \(1534\)](#); [Mars \(1007\)](#); [Pickup ions \(1239\)](#); [Plasma physics \(2089\)](#)

## 1. Introduction

Since the first detection of upstream waves near the local proton cyclotron frequency in the spacecraft frame at Mars, later known as proton cyclotron waves (PCWs), by the MAGMA magnetometer on board Phobos-2 (Russell et al. 1990), their specific properties, generation mechanisms, and generation conditions have been the subject of extensive observational studies and theoretical analyses (Brain et al. 2002; Mazelle et al. 2004; Wei & Russell 2006; Wei et al. 2011; Bertucci et al. 2013; Romanelli et al. 2013; Wei et al. 2014; Connerney et al. 2015b; Ruhunusiri et al. 2015; Romanelli et al. 2016; Ruhunusiri et al. 2016; Romeo et al. 2021). It is now well recognized that they are left-handed polarized in the spacecraft frame and propagate quasi-parallel with respect to the background magnetic field direction, and they are generated by a pickup process of protons upstream from Mars, originating from the extended hydrogen (H) exosphere of Mars. Specifically, the newly ionized protons through charge exchange, photoionization, and electron impact form a secondary ion population in the solar wind, and the interaction between the pickup ions and the solar wind plasma enables wave generation through ion/ion instabilities. Linear theories show that the electromagnetic ion–ion left-hand instability is the dominant mode when the interplanetary magnetic field (IMF) cone angle  $\alpha_{VB}$ , defined as the angle between the solar wind velocity ( $V$ ) and the IMF ( $B$ ), is very large and practically close to  $90^\circ$ , and the ion–ion right-hand

instability becomes dominant at small and moderate  $\alpha_{VB}$ . The transition from one type of instability to the other is proposed to occur around  $\alpha_{VB} = 70^\circ$  (Gary 1991). Both resonant instabilities could generate waves observed at the proton and other ion cyclotron frequencies in the spacecraft frame. So far, only waves near the local proton cyclotron frequency (i.e., PCWs) have been reported at Mars. This might be partly due to the fact that, in addition to the IMF cone angle, upstream wave generation depends on the relative density of the newborn exospheric ions to the background solar wind plasma (Bertucci et al. 2013; Romanelli et al. 2016). That is, the critical minimum value of the relative density required for efficient wave growth should be reached. It has been found that the relative density is even a key parameter for upstream PCW generation at Venus (Delva et al. 2011a, 2011b, 2015). Under stable solar wind conditions, the relative density at Mars is mainly related to the local exospheric H density and ionization frequency, which are known to show strong correlation with changes in the solar irradiance flux (Chaufray et al. 2015; Rahmati et al. 2018). Thus, a higher solar irradiance condition is expected to favor the generation of PCWs at Mars.

Observations support the expected contribution of the solar irradiance to the wave generation at Mars. For example, the occurrence rate of PCWs upstream from Mars exhibit a clear increasing trend with decreasing heliocentric distance, i.e., more PCWs near perihelion (close to the southern summer solstice) than around the spring and fall equinoxes, and this trend has been found to be closely correlated with the similar trend in the exospheric H density, as well as that in the solar irradiance reaching Mars (Bertucci et al. 2013; Yamauchi et al. 2015; Romanelli et al. 2016; Halekas 2017; Romeo et al. 2021). The annual trend of solar irradiance is essentially due to



Original content from this work may be used under the terms of the [Creative Commons Attribution 4.0 licence](#). Any further distribution of this work must maintain attribution to the author(s) and the title of the work, journal citation and DOI.

variations in the Martian heliocentric distance. In general, an increase in the solar irradiance can give rise to an increase in the photoionization frequency of the exospheric H atoms (Rahmati et al. 2018). Meanwhile, it can also influence the Martian atmosphere–ionosphere system, leading to the increase in the exospheric H density at high altitudes (Chaufray et al. 2015). Increased ionization of more H atoms in denser exospheric H near perihelion could increase the newborn proton production, and therefore the linear wave growth rate. This case clearly demonstrates that the increase in the solar irradiance facilitates the generation of PCWs near perihelion. It is worth noting that the increase in the solar irradiance can account for only a part of the increase of the occurrence rate of PCWs, because higher H exospheric density near perihelion originates from the combination of seasonal variations (Chaffin et al. 2014; Clarke et al. 2014; Bhattacharyya et al. 2015; Rahmati et al. 2018) and the solar irradiance trend (Romanelli et al. 2016; Romeo et al. 2021), rather than the solar irradiance trend alone.

In this Paper, we report a scenario of increased solar irradiance being the primary cause of the PCW generation upstream from Mars, as observed by Mars Atmosphere and Volatile Evolution (MAVEN; Jakosky et al. 2015). This scenario occurred in an X8.2 solar flare event on 2017 September 10, when the soft X-ray and EUV irradiances exhibited increases of up to 800% and 170%, respectively (Lee et al. 2018). It is the largest flare ever measured by MAVEN. Previous work has suggested that the Martian dust storm activity could have an effect on the variability of the H exosphere, and therefore upstream PCW generation (Romeo et al. 2021). During the period of the X8.2 flare, Mars was at a solar longitude  $L_s$  of  $59^\circ$ , corresponding to the late northern spring season on Mars, and close to Mars' aphelion. No global and regional dust storms erupted during this period (see Figure 1 of Fang et al. 2020), and therefore the PCW generation is not dust related. In addition, we find that no plasma waves were generated by instabilities associated with the increased production rate of newborn  $O^+$  ions during the flare. This might be due to the relatively low exospheric hot oxygen (O) density in the exosphere, compared to the exospheric H density (Rahmati et al. 2017).

## 2. MAVEN Data

The primary data used in this study are obtained from the Suprathermal and Thermal Ion Composition (STATIC) instrument (McFadden et al. 2015), the Magnetometer (MAG; Connerney et al. 2015a), the Solar Wind Ion Analyzer (SWIA; Halekas et al. 2015), and the solar Extreme Ultraviolet Monitor (EUVM; Eparvier et al. 2015) instruments on board MAVEN. STATIC operates over an energy range of 0.1 eV up to 30 keV, with a base time resolution of 4 s. It consists of a toroidal electrostatic analyzer with a  $360^\circ \times 90^\circ$  field of view (FOV), combined with a time-of-flight velocity analyzer with  $22.5^\circ$  resolution in the detection plane. The “d0” product, consisting of the mass, energy, and angle of ions with 16 azimuth bins, 4 elevation bins, and 8 mass bins, and with the time resolution of 128 s, is utilized to analyze ion velocity distribution functions (VDFs). The ions in the mass ranges of 0.75–1.25 and 12–20 are taken as  $H^+$  ions and  $O^+$  ions, respectively. MAG provides vector magnetic field measurements with a sampling frequency of 32 Hz with 0.05% absolute vector accuracy. SWIA is an energy and angular ion spectrometer with

electrostatic deflectors that measures ion fluxes. The ion moments are computed from the Fine 3D velocity distributions measured by SWIA under the assumption that all ions are protons. We utilize the onboard-computed ion velocity and energy spectra with 4 s time resolution. EUVM samples the solar irradiance in three broad wavelength bands (0.1–7 nm, 17–22 nm, and 121–122 nm) at a cadence of 1 s. The soft X-ray irradiance in 0.1–7 nm from the EUVM observations and EUV irradiance in 10–91 nm estimated from the Flare Irradiance Spectral Model for Mars (Thiemann et al. 2017) are used to characterize the flare irradiance. We also use the energy and angular distributions of 3–4600 eV electrons from the Solar Wind Electron Analyzer (SWEA) instrument (Mitchell et al. 2016), and the fluxes of electrons from 20 to 1000 keV, and ions from 20 to 6000 keV measured by the solar energetic particle (SEP) instrument (Larson et al. 2015).

## 3. Observation and Analysis

Figure 1 shows MAVEN measurements during the period 09:00–18:00 UT on 2017 September 10, including two upstream solar wind segments ( $\sim 10:10$ – $11:50$  UT and  $\sim 15:10$ – $16:51$  UT) when MAVEN orbit (orbit 5716 and orbit 5717) extended out of the Martian bow shock (BS). Orbit 5716 and orbit 5717 start at the periapsis passage times of 08:50 UT and 13:16 UT, respectively. During orbit 5716, the outbound and inbound BS crossings are clearly distinguished by abrupt increases in magnetic field magnitude and fluctuation level, a sharp decrease in bulk flow velocity, along with a pronounced broadening of ion energy spectra across the BS from the upstream to the downstream, which are characteristics of the bow shock crossing for each orbit. During orbit 5717, the outbound BS crossing is less clear. We consider that it occurred around 15:10 UT, when the ion energy spectra became narrow and the flow was deflected to the negative  $Z$  direction in Mars Solar Orbital (MSO) coordinates. In contrast, the inbound BS crossing is very evident. It is characterized by an abrupt increase in magnetic field magnitude and a pronounced broadening of ion and electron energy spectra, and thus provides strong evidence that MAVEN entered the upstream solar wind during orbit 5717. We note that the spatial position of the inbound BS crossing of orbit 5717 is far away from that of orbit 5716, implying large changes in the location and shape of the Martian BS. The changes might be partly due to the enhanced solar irradiance from the X8.2 flare. It should be mentioned that, the MAVEN orbit did not extend outside of the Martian BS during the surrounding orbits (5714, 5715, 5718, and 5719), mainly owing to the changes of the location and shape of the Martian BS caused by both external and internal drivers (Garnier et al. 2022). The present study focuses on the observations upstream from the BS during orbits 5716 and 5717.

The X8.2 flare was detected at Mars by EUVM. It started in the soft X-ray irradiance (0.1–7 nm) and EUV irradiance (10–91 nm) at about 15:50 UT and peaked near 16:15 UT (Figure 1(a)), which preceded the orbit 5717 inbound BS crossing at 16:51 UT by about 36 minutes. The flare X-rays were also recorded by the SEP instrument in its “thick” detector during the interval 16:00–16:15 UT (Figure 1(d)). To investigate the potential influence of the flare on the generation of pickup ions via ionization of exospheric neutral atoms upstream of the Martian BS, particularly the H atoms and hot O atoms that populate the Martian exosphere and can escape to

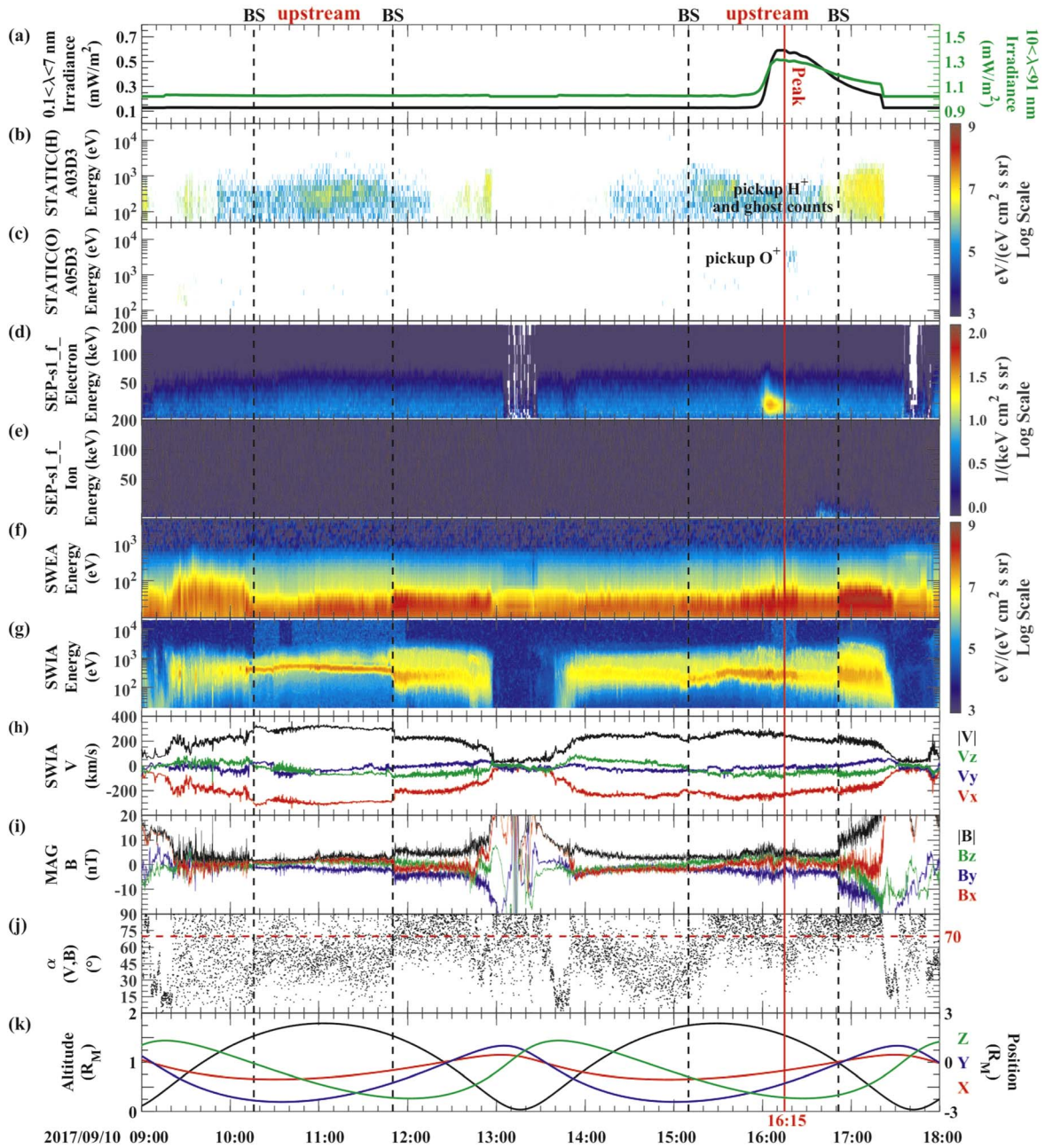


**Figure 1.** In situ observations from MAVEN during the period 09:00-18:00 UT on 2017 September 10, encompassing an X8.2 solar flare. From top to bottom: (a) EUVM solar soft X-ray (0.1–7 nm) and EUV (10–91 nm) irradiance, (b) energy fluxes of pickup  $H^+$  in one of the look directions of STATIC, namely, A03D3, (c) energy fluxes of pickup  $O^+$  in one of the look direction bins of STATIC, namely, A05D3, (d) SEP electron energy spectra in the forward look direction, (e) SEP ion energy spectra in the forward look direction, (f) SWEA electron energy spectra, (g) SWIA ion energy spectra, (h) proton velocity components in MSO coordinates and bulk proton speed from SWIA, (i) magnetic field components in MSO coordinates and magnetic field magnitude measured by MAG, (j) the IMF cone angle, defined as the angle between the solar wind velocity and the interplanetary magnetic field (IMF), and (k) the MAVEN spacecraft altitude and position in units of the radius of Mars  $R_M$ . Vertical dotted-dashed lines mark the Martian bow shock (BS) crossings. The red vertical line indicates the time of flare peak (at  $\sim 16:15$  UT).

space when they obtain energies above the escape energy, we examine the ion energy spectral in all 64 look directions of STATIC and SWIA, i.e., 16 azimuth bins of  $22.5^\circ$  and 4 elevation bins of  $22.5^\circ$ . The measurements by SEP are not considered here, because the solar wind speed during the flare period is too low for  $H^+$  and  $O^+$  pickup ions to gain enough energy to be detectable by SEP. In SWIA spectrograms (not shown), reflected  $H^+$  ions from the Martian BS are clearly visible, whereas  $H^+$  pickup ions are masked by ghost ions (i.e., the scattered solar wind ions in the instrument) and therefore barely identifiable. In addition,  $O^+$  pickup ions are not readily

identifiable. A careful analysis of STATIC spectrograms suggests that a larger number of  $O^+$  ions entered the FOV of STATIC around the flare peak. As an example, Figure 1(c) shows the measured pickup  $O^+$  populations in one of the look direction bins of STATIC, namely, A05D3, which do not have the solar wind ions. The pickup  $O^+$  fluxes around the flare peak are much higher than those in quiescence with similar upstream plasma conditions during orbits 5716 and 5717. The enhanced pickup  $O^+$  fluxes are mainly due to the additional ionization caused by the flare, and the FOV effects might be also involved, e.g., the change in the IMF direction takes  $O^+$  pickup

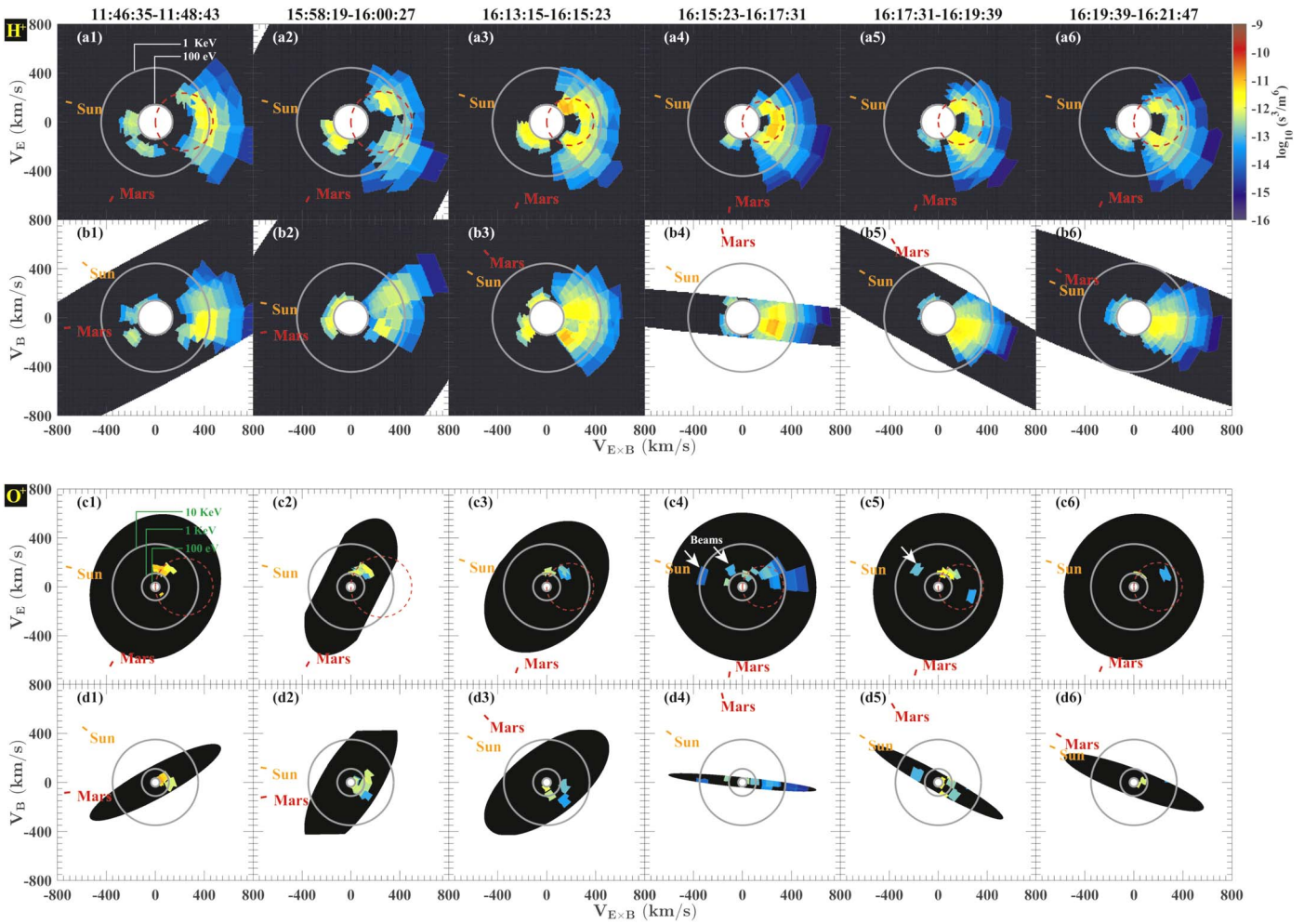


**Figure 2.**  $H^+$  and  $O^+$  VDFs based on the STATIC “d0” product. (a1)–(a6) and (b1)–(b6) panels represent  $H^+$  VDFs projected on the plane perpendicular to the local magnetic field and to the convection electric field, respectively. Gray circles correspond to contours of 100 eV and 1 keV, respectively. (c1)–(c6) and (d1)–(d6) panels represent  $O^+$  VDFs projected on the plane perpendicular to the local magnetic field and to the convection electric field, respectively. Gray circles correspond to contours of 100 eV, 1 keV, and 10 keV, respectively. The red dashed circle in (a1)–(a6) and (c1)–(c6) panels corresponds to a ring distribution calculated by local proton bulk velocity perpendicular to the local magnetic field. The white arrows in (c4) and (c5) mark the energetic  $O^+$  ion beams.

ions in and out of the FOV of each bin. As we will see later, the additional ionization essentially results from both an increase of the hot O density and an increase of the photoionization frequency of hot O atoms. The increase of pickup  $O^+$  fluxes is a good indicator that the ionization of neutral exosphere was intensified due to the flare, and gives us confidence that a similar increase in the pickup  $H^+$  fluxes occurred around the flare peak, although are barely visible in the spectra due to ghost count contamination.

To further understand the dynamics of flare-induced pickup ions in the upstream solar wind, we analyze their VDFs measured by STATIC. We use the data product of “d0” with a time resolution of 128 s in this period. Figures 2(a1)–(a6) and Figures 2(b1)–(b6), respectively, show the characteristic  $H^+$  ion VDFs projected on the plane perpendicular to the local magnetic field and to the convection electric field ( $E = -V \times B$ ;  $V$  is the local proton velocity vector and  $B$  is the local magnetic field vector) at different times corresponding to the preflare phase ( $\sim 11:47$  UT), the initiation phase ( $\sim 15:59$  UT), around flare peak ( $\sim 16:16$  UT), and shortly after the flare peak ( $\sim 16:18$  UT and  $\sim 16:20$  UT). It is known that the  $H^+$  ion VDFs have a denser solar wind proton core component (e.g., Marsch et al. 1982). Here, the core component with radii of 0.6

times proton bulk velocity  $V_{\perp}$  perpendicular to the local IMF in the velocity space is arbitrarily removed, by referring to the dependence of the phase space density of solar wind protons on the solar wind speed measured with SWICS (Gloeckler et al. 1995; Schwadron & Gloeckler 2007). We note that  $H^+$  pickup ions located on the ring distribution in the VDFs, as indicated by the red dashed circles calculated by local proton bulk velocity  $V_{\perp}$  perpendicular to the local IMF, are often contaminated by ghost ions as well as a part of solar wind protons. Thus the signatures of additional  $H^+$  pickup ions due to the flare are hardly identified by tracing the temporal evolution of the VDF.

Figures 2(c1)–(c6) and (d1)–(d6) show the  $O^+$  ion VDFs in the same format as Figures 2(a1)–(a6) and (b1)–(b6), respectively. It is immediately clear that two pronounced changes in the  $O^+$  ion VDF occur around the flare peak (Figure 2(c4)). First, the  $O^+$  pickup ions measured at  $\sim 16:16$  UT have a velocity phase in the first and second quadrants of the ring distribution, compared to a velocity phase near the initial phase of the ring distribution in quiescence. This change could be essentially attributed to the enhanced pickup  $O^+$  fluxes due to the additional ionization caused by the flare. The  $O^+$  pickup ions on the ring distribution could mainly originate

in the far extended O corona above the BS. Certainly, it is possible that a part of the O<sup>+</sup> pickup ions corresponding to the early velocity phase of the ring distribution (i.e., the so-called “plume” ions; Fang et al. 2008; Dong et al. 2015) could originate from the ionosphere. Second, sunward O<sup>+</sup> ion beams with energy of several to  $\sim 10$  keV are present at  $\sim 16:16$  UT, as marked by arrows in Figure 2(c4). The incident O<sup>+</sup> ion beams can be interpreted in terms of the reflection of precipitating O<sup>+</sup> pickup ions in the Martian magnetosheath by the strong magnetic field and convection electric field, as proposed by Masunaga et al. (2016, 2017). As shown in Figure 1(i), the magnetosheath magnetic field along the flare orbit was intensified by a factor of 2 or more, compared to the preflare level. The enhanced magnetosheath magnetic field could be the main cause of the reflection of precipitating O<sup>+</sup> pickup ions. The O<sup>+</sup> pickup ions might be initially created through the solar flare additional ionization of exospheric hot O atoms above the BS.

To explore whether the solar flare additional ionization induced the generation of ion cyclotron waves upstream from the BS, we perform a detailed analysis of the magnetic field perturbations. The 32 Hz magnetic field data are transformed from MSO coordinates to local mean field-aligned (MFA) coordinates (e.g., Takahashi et al. 1990), in which the parallel unit vector  $B_{\text{par}}$  is parallel to the 3 minute running average magnetic field vector, the azimuthal unit vector  $B_{\text{azi}}$  is along the cross product of  $B_{\text{par}}$ , and the Mars-centered radial vector to the spacecraft position. Then, the generalized Morse wavelets (Olhede & Walden 2002) are employed on the transverse ( $B_{\text{TRA}}$ ) and compressive ( $B_{\text{COMP}}$ ) components. Figures 3(a)–(e) show the magnetic field time series in MFA coordinates and wavelet spectrum for the interval 16:11:00–16:20:00 UT, covering the main phase of the flare. We can see clearly that the transverse ( $B_{\text{TRA}}$ ) component exhibits a pronounced spectral density peak in the frequency range of 0.072–0.116 Hz (marked by two horizontal dashed lines) with a center frequency of  $\sim 0.094$  Hz during the subinterval 16:15:25–16:16:15 UT, i.e., around the flare peak. The center frequency is very close to the local proton cyclotron frequency of  $\sim 0.089$  Hz ( $f_{H^+} = q|B|/2\pi m$ , where  $q$  and  $m$  denote the proton charge and mass, respectively), as indicated by the white solid line. Such a spectral density peak is almost invisible in the wavelet spectrum of the compressive ( $B_{\text{COMP}}$ ) component. This implies the presence of transverse waves near the local proton cyclotron frequency associated with the flare additional ionization. Nevertheless, similar waves near the O<sup>+</sup> ion cyclotron frequency are not presented. To analyze the polarization and propagation direction of the waves, we apply a minimum variance analysis (MVA) to both the raw and the bandpass-filtered (0.072–0.116 Hz) magnetic field data for the subinterval 16:15:25–16:16:15 UT. Figures 3(f)–(h) show the magnetic components in the lmn coordinates, which correspond to the maximum, intermediate, and minimum variance direction of magnetic field ( $Bl$ ,  $Bm$ , and  $Bn$ ), respectively, and Figures 3(i)–(j) show the hodographs in the  $Bl - Bm$  and  $Bl - Bn$  planes, respectively. For the filtered data (the raw data), the ratios of maximum to intermediate and intermediate to minimum eigenvalues are 1.34 and 11.8 (1.50 and 3.0), respectively. It implies that the waves are nearly circularly polarized and planar. The mean magnetic field in the MVA basis is  $B_0 = [0.27, -0.17, 5.25]$  nT, pointing out of the  $Bl - Bm$  plane. The sense of gyration of the filtered magnetic

field oscillations with respect to  $B_0$ , indicated by a green arrow arc (Figure 3(i)), demonstrates that the waves are left-hand polarized in the spacecraft frame. The minimum variance direction is taken to be coincident with the direction of the wavevector  $k$  here (note that there is a  $180^\circ$  ambiguity in determining the wave direction), and then the propagation angle  $\theta_{\text{kB}}$  between the wavevector  $k$  and the mean magnetic field  $B_0$  is estimated to be  $\sim 3^\circ$ . It indicates that the waves propagate either sunward or antisunward closely parallel to the ambient magnetic field direction. Since the waves possess a set of desirable properties of PCWs upstream from Mars, they can be unambiguously identified as PCWs. Moreover, they are the only upstream waves that can be identified as PCWs during orbits 5716 and 5717. It should be mentioned that the left-hand polarized waves here appear as a wave packet already strongly affected by nonlinear effects (steepening with a possible generation of higher frequencies by dispersive effects) and do not appear as nearly monochromatic waves as the “classical” PCWs observed during the most favorable period (around solar longitude  $L_s$  of  $270^\circ$  whereas here  $L_s = 59^\circ$ , so not far from the minimum season around  $90^\circ$  for the H exosphere). That would explain the exceptional evidence of such waves in this season consistent with the impact of the flare. That would also mean the waves already evolved a lot from the linear phase and that their source is further upstream in the solar wind (being convected back by the solar wind, as mentioned later). That means the exospheric H<sup>+</sup> density must be already strongly increased by the flare at larger distances from Mars than the wave observation location.

As mentioned earlier, in principle, PCWs can be generated by either an ion/ion left-hand resonant instability or an ion/ion right-hand resonant instability fed by planetary H<sup>+</sup> pickup ions, depending on the IMF cone angle. During the interval of this PCW event, the IMF cone angle lay in the range  $30^\circ$ – $60^\circ$ , and thus the dominant mechanism that gave rise to the wave growth should be the ion/ion right-hand resonant instability. It indicates that, in the solar wind frame, the sunward H<sup>+</sup> pickup ions overtook and interacted via anomalous cyclotron resonances with the costreaming waves (see Mazelle & Neubauer 1993; Mazelle et al. 2004), transferring energy from the H<sup>+</sup> pickup ions into resonant waves. The waves are intrinsically right-handed in the solar wind frame, possibly corresponding to the magnetosonic mode at frequencies below the proton cyclotron frequency, but they were detected by MAVEN MAG in the spacecraft frame as left-hand polarized waves nearly at local proton cyclotron frequency. The waves only lasted about 4–5 proton cyclotron periods (Figures 3(f) and (g)), implying a transient appearance of favorable plasma and exospheric conditions for wave growth. Referring back to Figure 1, the background solar wind plasma and IMF conditions did not undergo significant temporal variabilities around the solar flare peak. It seems more likely that, in response to the sudden enhancement of the solar irradiance, the relative pickup H<sup>+</sup> density to the background plasma was increased up to the values sufficient for wave growth. This raises a question of how the densities of H atoms and hot O atoms in the Martian exosphere respond to the flare. During the flare peak of interest in this study, MAVEN was located in the solar wind and therefore did not closely observe the response of the atmosphere–ionosphere system and the variability of the Martian exosphere. Extensive modeling efforts have been conducted to understand the ionospheric and thermospheric

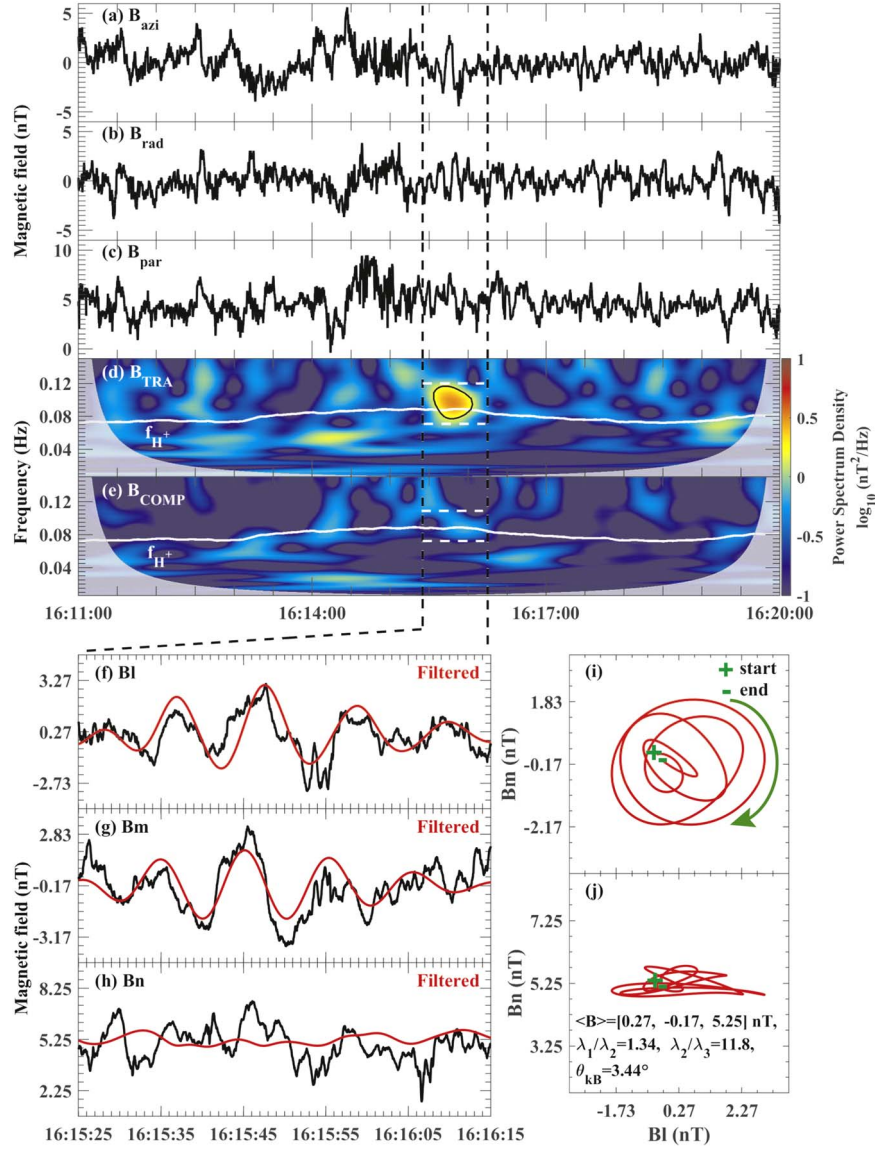


**Figure 3.** Observation and identification of proton cyclotron waves occurred just after the flare peak. ((a)–(c)) The azimuthal ( $B_{azi}$ ), radial ( $B_{rad}$ ), and parallel ( $B_{par}$ ) components of the magnetic field in the local MFA coordinate system during 16:11:00–16:20:00 UT. ((d)–(e)) Morse wavelet spectrum of the magnetic field transverse ( $B_{TRA}$ ) and compressive ( $B_{COMP}$ ) components. The thick black contour designates the 95% confidence level against red noise and the cone of influence where edge effects might distort the picture is shown as a lighter shade. The white solid line indicates the mean local proton cyclotron frequency ( $f_{H^+}$ ). ((f)–(h)) Raw (black) and bandpass-filtered (red) magnetic field components in the maximum variance, intermediate variance, and minimum variance directions (i.e.,  $B_l$ ,  $B_m$  and  $B_n$ ) during 16:15:25–16:16:15 UT. The mean value is added to the filtered data for comparison with the raw data. The filter has cutoff frequencies at 0.072 and 0.116 Hz, which are determined by the wavelet power spectrum (marked by the white dashed lines in panels (d) and (e)). ((i) and (j)) Hodogram of filtered  $B_l$  and  $B_m$  and that of filtered  $B_l$  and  $B_n$  displayed in panels (f)–(h). The plus and minus symbols refer to the beginning and the end of the time series. The ratio of the maximum to the intermediate eigenvalue ( $\lambda_1/\lambda_2$ ) and that of the intermediate to the minimum eigenvalue ( $\lambda_2/\lambda_3$ ), the mean magnetic field, and the estimated propagation angle  $\theta_{kB}$  are shown.

behaviors during the flare (Lee et al. 2018; Thiemann et al. 2018; Xu et al. 2018; Fang et al. 2019; Cramer et al. 2020). In general, the models are first validated by comparing their results to MAVEN measurements of the Martian upper atmosphere and ionosphere along preflare and near-post-flare orbits. Based on current knowledge of the ionospheric and thermospheric responses to this flare event from a variety of MAVEN data productions and numerical models, this question will be discussed below.

#### 4. Discussion

It is generally known that the main source of hot and escaping O atoms in the Martian exosphere is the dissociative

recombination of  $O_2^+$  ions with electrons in the ionosphere (Nagy & Cravens 1988; Kim et al. 1998). A simulation study conducted by Lee et al. (2018) suggests that, when the flare begins to impact the atmosphere and ionosphere of Mars, the hot O density increases rapidly and reaches its maximum almost simultaneously with the flare peak, without apparent changes in the spatial structure. The transient enhancement of the hot O density around the flare peak is mainly attributed to the rapid increase of the ionospheric electron density due to fast photochemical reactions, which in turn intensifies the dissociative recombination of  $O_2^+$  ions with ambient electrons and therefore the production of hot O. On the other hand, the response of the neutral atmosphere through accumulation and

redistribution processes, involving atmospheric heating, photochemistry, and transport (Cramer et al. 2020), is much slower and longer lasting (Thiemann et al. 2015). It takes  $\sim 2.5$  hr to reach the perturbation peak and then an additional  $\sim 10$ – $18$  hr to return to the preflare state (Lee et al. 2018; Fang et al. 2019), and thus a quick thermalization of the nascent hot O in the high collisional environment is avoided. It is important to point out that, the ionospheric electron density enhancement at altitudes below the main ionospheric peak is mainly caused by the sudden increase of solar X-ray flux; but it could not contribute to the density of the hot oxygen atoms and the flux of the  $O^+$  pickup ions above the BS, because almost all the escalated hot O are thermalized before escape. In contrast, the increase of the electron density at high altitudes is mainly due to the simultaneous increase in the EUV irradiance; it makes a major contribution to the enhancement in hot O production, which helps in populating a relatively denser hot O exosphere (Lee et al. 2018). Additional ionization of the more abundant hot O atoms creates more  $O^+$  pickup ions upstream of the BS, which were indeed detected by STATIC. These facts help to explain why higher pickup  $O^+$  fluxes occurred around the flare peak, meanwhile, suggesting that they resulted not only from the increase of the photoionization frequency but also from the increase of the hot O density. However, despite more  $O^+$  pickup ions created in response to the flare, the relative density of the newborn  $O^+$  ions with respect to the background solar wind might be still insufficient to enable  $O^+$  ion cyclotron wave generation.

One can expect a corresponding increase in the density of hot O atoms with kinetic energy high enough to escape from Mars, i.e., the escaping hot O atoms, which are dominant in the distant exosphere, typically above  $\sim 10 R_M$  (Rahmati et al. 2014). The escaping hot O atoms can also be ionized and picked up by the solar wind, and then be energized by the solar wind motional electric field. Rahmati et al. (2014) suggested that, when  $O^+$  pickup ions are energized to above  $\sim 60$  keV, they will become detectable by MAVEN SEP. Nevertheless, such a scenario did not take place during this flare event, owing to relatively lower solar wind speed (slower than  $\sim 450$  km  $s^{-1}$ ). It remains to be confirmed by the ongoing MAVEN observations.

The H exosphere at Mars is populated by thermal H atoms, which are mostly produced by the photodissociation of  $H_2O$  in the lower atmosphere below  $\sim 20$  km (McElroy & Donahue 1972; Parkinson & Hunten 1972). Molecular hydrogen  $H_2$  can be formed in the lower atmosphere by three-body H recombination with  $CO_2$  as a collision partner and in middle atmosphere at about 20–50 km by the reaction between H and  $HO_2$  (Krasnopolsky & Feldman 2001). As a result of atmospheric mixing and diffusion,  $H_2$  is transported to the upper atmosphere, where it can be convected back into atomic H mainly through reaction with  $CO_2^+$  and subsequent dissociative recombination of  $HCO_2^+$ . In addition, many other chemical reactions, involving ion–molecular reactions, ionization (followed by ion reactions), and photoelectron dissociation (see Krasnopolsky 2002), can also contribute to the formation and loss of H and  $H_2$  in the upper atmosphere. Thus the behavior of H and  $H_2$  with varying solar activity is very complicated. The vertical profiles of all components of interest under different solar activity conditions are solved self-consistently in a 1D model of neutral and ion composition at 80–400 km by Krasnopolsky (2010), who predicted a slight

decrease of the H and  $H_2$  densities above 150 km with the increasing solar activity. MAVEN observations and atmospheric models indicate that, in response to the solar irradiance enhancement during the flare, the neutral temperatures increase by 70–100 K (Elrod et al. 2018; Jain et al. 2018), and the densities of heavy species (with masses greater than  $\sim 4$  atomic mass units, such as  $CO_2$ , O,  $N_2$ , CO, and Ar) increase by a factor of 2.5–5 at fixed altitude (Elrod et al. 2018; Fang et al. 2019). However, the densities of the lighter species like H, decrease slightly during the flare. An atmospheric modeling study by Mayyasi et al. (2018) indicates a 25% decrease in H density at the exobase (around 200–250 km) during the flare. This result is consistent with previous simulations conducted with a 1D model by Krasnopolsky (2010) and a 3D model by Chaufray et al. (2015). The 3D model also predicted an increase of the H density in the upper exosphere (e.g., above  $\sim 4000$  km) with increasing solar activity. Thus, it is reasonable to suggest that the exospheric H density above the BS underwent an increase during the flare, although whether it reached the maximum almost simultaneously with the flare peak remains unknown. The increase of the exospheric H density above the BS, together with the simultaneous increase of the photoionization frequency of H atoms, gave rise to the increase of the pickup  $H^+$  fluxes, and in turn induced the generation of the observed PCW event.

## 5. Conclusions

During the X8.2 solar flare on 2017 September 10, the soft X-ray and EUV irradiances at Mars increased up to 800% and 170%, respectively. In response to the significant increase in the solar irradiance, the exospheric hot O and H densities above the Martian bow shock and the ionization rate of exospheric neutral atoms were increased, leading to higher pickup  $O^+$  and  $H^+$  fluxes, which were detected by MAVEN STATIC around the flare peak. The latter in turn induced proton cyclotron waves (PCWs), lasting about 4–5 proton cyclotron periods. The waves might be generated by the interaction between the solar wind plasma and the pickup  $H^+$  through ion/ion right-hand instabilities. Thus they are intrinsically right-handed in the solar wind frame, possibly corresponding to magnetosonic mode at frequencies below the proton cyclotron frequency, but they were detected by MAVEN MAG in the spacecraft frame as left-hand polarized waves nearly at local proton cyclotron frequency. This is the first in situ evidence for flare-induced PCWs upstream from Mars. This event brings new insight toward understanding the PCW generation conditions, and also has profound implications for loss of hydrogen to space in early Martian history, when large solar flares are believed to occur more frequently, and their contributions to the total loss.

This work is supported by the Strategic Priority Research Program of Chinese Academy of Sciences, grant No. XDB 41000000, the National Natural Science Foundation of China (NSFC; 42074212), the pre-research Project on Civil Aerospace Technologies No. D020104 funded by Chinese National Space Administration, the Key Research Program of the Institute of Geology and Geophysics, CAS, grant IGGCAS-201904. The multi-instrument MAVEN data set used in this work is publicly available at the Planetary Data System Planetary Plasma Interactions Node (<https://pds-ppi.igpp.ucla.edu/>).

## ORCID iDs

Haibo Lin  <https://orcid.org/0000-0002-3530-3402>  
 Jianpeng Guo  <https://orcid.org/0000-0003-1707-2716>  
 Kei Masunaga  <https://orcid.org/0000-0001-9704-6993>  
 Kanako Seki  <https://orcid.org/0000-0001-5557-9062>  
 Christian Mazelle  <https://orcid.org/0000-0001-5332-9561>  
 Dan Zhao  <https://orcid.org/0000-0001-8962-5397>  
 Hui Huang  <https://orcid.org/0000-0001-7098-551X>  
 Yong Wei  <https://orcid.org/0000-0001-7183-0229>  
 Libo Liu  <https://orcid.org/0000-0001-5773-0184>

## References

- Bertucci, C., Romanelli, N., Chaufray, J. Y., et al. 2013, *GeoRL*, **40**, 3809  
 Bhattacharyya, D., Clarke, J. T., Bertaux, J.-L., Chaufray, J.-Y., & Mayyasi, M. 2015, *GeoRL*, **42**, 8678  
 Brain, D. A., Bagenal, F., Acuña, M. H., et al. 2002, *JGRA*, **107**, 1076  
 Chaffin, M. S., Chaufray, J.-Y., Stewart, I., et al. 2014, *GeoRL*, **41**, 314  
 Chaufray, J. Y., Gonzalez-Galindo, F., Forget, F., et al. 2015, *Icar*, **245**, 282  
 Clarke, J. T., Bertaux, J. L., Chaufray, J. Y., et al. 2014, *GeoRL*, **41**, 8013  
 Connerney, J. E. P., Espley, J., Lawton, P., et al. 2015a, *SSRv*, **195**, 257  
 Connerney, J. E. P., Espley, J. R., DiBraccio, G. A., et al. 2015b, *GeoRL*, **42**, 8819  
 Cramer, A. G., Withers, P., Elrod, M. K., Benna, M., & Mahaffy, P. R. 2020, *JGRA*, **125**, e28518  
 Delva, M., Bertucci, C., Volwerk, M., et al. 2015, *JGRA*, **120**, 344  
 Delva, M., Mazelle, C., & Bertucci, C. 2011a, *SSRv*, **162**, 5  
 Delva, M., Mazelle, C., Bertucci, C., et al. 2011b, *JGRA*, **116**, A02318  
 Dong, Y., Fang, X., Brain, D. A., et al. 2015, *GeoRL*, **42**, 8942  
 Elrod, M. K., Curry, S. M., Thiemann, E. M. B., & Jain, S. K. 2018, *GeoRL*, **45**, 8803  
 Eparvier, F. G., Chamberlin, P. C., Woods, T. N., & Thiemann, E. M. B. 2015, *SSRv*, **195**, 293  
 Fang, X., Liemohn, M. W., Nagy, A. F., et al. 2008, *JGRA*, **113**, A02210  
 Fang, X., Ma, Y., Lee, Y., et al. 2020, *JGRA*, **125**, e26838  
 Fang, X., Pawlowski, D., Ma, Y., et al. 2019, *GeoRL*, **46**, 9334  
 Garnier, P., Jacquey, C., Gendre, X., et al. 2022, *JGRA*, **127**, e30147  
 Gary, S. P. 1991, *SSRv*, **56**, 373  
 Gloeckler, G., Schwadron, N. A., Fisk, L. A., & Geiss, J. 1995, *GeoRL*, **22**, 2665  
 Halekas, J. S. 2017, *JGRE*, **122**, 901  
 Halekas, J. S., Lillis, R. J., Mitchell, D. L., et al. 2015, *GeoRL*, **42**, 8901  
 Jain, S. K., Deighan, J., Schneider, N. M., et al. 2018, *GeoRL*, **45**, 7312  
 Jakosky, B. M., Lin, R. P., Grebowsky, J. M., et al. 2015, *SSRv*, **195**, 3  
 Kim, J., Nagy, A. F., Fox, J. L., & Cravens, T. E. 1998, *JGR*, **103**, 29339  
 Krasnopolsky, V. A. 2002, *JGRE*, **107**, 5128  
 Krasnopolsky, V. A. 2010, *Icar*, **207**, 638  
 Krasnopolsky, V. A., & Feldman, P. D. 2001, *Sci*, **294**, 1914  
 Larson, D. E., Lillis, R. J., Lee, C. O., et al. 2015, *SSRv*, **195**, 153  
 Lee, Y., Dong, C., Pawlowski, D., et al. 2018, *GeoRL*, **45**, 6814  
 Marsch, E., Schwenn, R., Rosenbauer, H., et al. 1982, *JGR*, **87**, 52  
 Masunaga, K., Seki, K., Brain, D. A., et al. 2016, *JGRA*, **121**, 3093  
 Masunaga, K., Seki, K., Brain, D. A., et al. 2017, *JGRA*, **122**, 4089  
 Mayyasi, M., Bhattacharyya, D., Clarke, J., et al. 2018, *GeoRL*, **45**, 8844  
 Mazelle, C., & Neubauer, F. M. 1993, *GeoRL*, **20**, 153  
 Mazelle, C., Winterhalter, D., Sauer, K., et al. 2004, *SSRv*, **111**, 115  
 McElroy, M. B., & Donahue, T. M. 1972, *Sci*, **177**, 986  
 McFadden, J. P., Kortmann, O., Curtis, D., et al. 2015, *SSRv*, **195**, 199  
 Mitchell, D. L., Mazelle, C., Sauvaud, J. A., et al. 2016, *SSRv*, **200**, 495  
 Nagy, A. F., & Cravens, T. E. 1988, *GeoRL*, **15**, 433  
 Olhede, S. C., & Walden, A. T. 2002, *ITSP*, **50**, 2661  
 Parkinson, T. D., & Hunten, D. M. 1972, *JAtS*, **29**, 1380  
 Rahmati, A., Cravens, T. E., Nagy, A. F., et al. 2014, *GeoRL*, **41**, 4812  
 Rahmati, A., Larson, D. E., Cravens, T. E., et al. 2017, *JGRA*, **122**, 3689  
 Rahmati, A., Larson, D. E., Cravens, T. E., et al. 2018, *JGRE*, **123**, 1192  
 Romanelli, N., Bertucci, C., Gómez, D., Mazelle, C., & Delva, M. 2013, *P&SS*, **76**, 1  
 Romanelli, N., Mazelle, C., Chaufray, J. Y., et al. 2016, *JGRA*, **121**, 11,113  
 Romeo, O. M., Romanelli, N., Espley, J. R., et al. 2021, *JGRA*, **126**, e28616  
 Ruhunusiri, S., Halekas, J. S., Connerney, J. E. P., et al. 2015, *GeoRL*, **42**, 8917  
 Ruhunusiri, S., Halekas, J. S., Connerney, J. E. P., et al. 2016, *JGRA*, **121**, 2374  
 Russell, C. T., Luhmann, J. G., Schwingenschuh, K., Riedler, W., & Yeroshenko, Y. 1990, *GeoRL*, **17**, 897  
 Schwadron, N. A., & Gloeckler, G. 2007, *SSRv*, **130**, 283  
 Takahashi, K., McEntire, R. W., Lui, A. T. Y., & Potemra, T. A. 1990, *JGR*, **95**, 3717  
 Thiemann, E. M. B., Andersson, L., Lillis, R., et al. 2018, *GeoRL*, **45**, 8005  
 Thiemann, E. M. B., Chamberlin, P. C., Eparvier, F. G., et al. 2017, *JGRA*, **122**, 2748  
 Thiemann, E. M. B., Eparvier, F. G., Andersson, L. A., et al. 2015, *GeoRL*, **42**, 8986  
 Wei, H. Y., Cowee, M. M., Russell, C. T., & Leinweber, H. K. 2014, *JGRA*, **119**, 5244  
 Wei, H. Y., & Russell, C. T. 2006, *GeoRL*, **33**, L23103  
 Wei, H. Y., Russell, C. T., Zhang, T. L., & Blanco-Cano, X. 2011, *P&SS*, **59**, 1039  
 Xu, S., Fang, X., Mitchell, D. L., et al. 2018, *GeoRL*, **45**, 7337  
 Yamauchi, M., Hara, T., Lundin, R., et al. 2015, *P&SS*, **119**, 54